

# Generalized Analytical Solar Radiation Pressure Modeling Algorithm for Spacecraft of Complex Shape

Marek Ziebart\*

University College London, London, England WC1E 6BT, United Kingdom

The theoretical background of solar radiation pressure modeling is presented. The attitude behavior of specific classes of spacecraft and how these attitudes make it feasible to model radiation pressure effects in the spacecraft body-fixed coordinate system are explained. The core mathematical and computational elements of the radiation pressure modeling algorithm are described. Specific components of the algorithm that enable the accurate modeling of curved surfaces and the speed optimization of the computational process are detailed. The methods and results of various forms of validation of the modeling method are given. The principal benefits of the method are that it can deal with realistic and complex spacecraft structures easily and efficiently and that it enables forms of analysis that were previously impossible. These include modeling the effects of how radiation reflected from the spacecraft surface can strike other parts of the structure causing further acceleration and simulating the effects of anomalous forces caused by departure from the spacecraft's nominal attitude regime.

## Nomenclature

$A$	=	surface area of a surface component, $m^2$
$A_\lambda$	=	coefficient of squared term in locus of principal section of paraboloid
$a$	=	coefficient of squared term in locus of displaced paraboloid section
$b_1$ – $b_4$	=	quaternion components
$C$	=	constant term in locus of principal section of paraboloid
$c$	=	constant term in locus of displaced paraboloid section
$c_{EM}$	=	speed of light in vacuum, $ms^{-1}$
$d$	=	depth of paraboloid, $m$
$E$	=	total solar irradiance, $J \cdot s^{-1} m^{-2}$
$F$	=	force, $N$
$f$	=	frequency, $Hz$
$h$	=	Planck's constant, $J \cdot s^{-1}$
$m_0$	=	rest mass of particle, $kg$
$n(f)$	=	average number of solar photons of frequency $f$ striking unit area of surface at one astronomical unit
$\hat{n}$	=	unit vector normal to surface
$P$	=	$A E \cos \theta / c_{EM}$
$p$	=	momentum of particle, $kgm \cdot s^{-1}$
$\hat{q}$	=	light ray vector
$\hat{q}_i$	=	quaternion rotation axis
$R_i$	=	rotation matrix
$r$	=	radius of open end of parabola, $m$
$\hat{s}$	=	surface shear vector
$t$	=	time, $s$
$x_c$	=	position vector of center of open end of paraboloid
$x_d$	=	position vector of closed end of paraboloid
$x_p$	=	position vector of start point of light ray vector
$x_i$	=	position vector of endpoint of light ray vector
$\beta$	=	angle between the instantaneous orbital plane and the sun position vector
$\delta$	=	angle by which the sun is apparently rotated with respect to the satellite
$\varepsilon$	=	energy of particle, $J$
$\theta$	=	angle of incidence of radiation

$\theta_{EPS}$	=	Earth–probe–sun angle
$\kappa$	=	rotation angle about basis $Z$ axis
$\mu$	=	surface material specularity, the proportion of reflected radiation that is reflected specularly, that is, where the surface behaves as a perfect mirror
$\nu$	=	surface material reflectivity, the proportion of incident radiation that is reflected
$\phi$	=	rotation angle about basis $Y$ axis

## Introduction

MANY space-based scientific and commercial applications require highly accurate orbit information for the system spacecraft. These spacecraft range from global navigation satellite system (GNSS) medium-Earth-orbit (MEO) satellites down to low-Earth-orbit (LEO) satellite altimetry and synthetic aperture radar missions. The calculation of the orbits relies fundamentally on accurate modeling of the forces acting on the spacecraft. The principal components of the force field in the MEO and LEO environments are due to Earth gravity and the third body effects of lunar and solar gravity. In the hierarchy of force magnitudes the next most important force for all MEO, and many LEO, spacecraft is due to solar radiation pressure (SRP). SRP is the force caused by the impact of solar photons on the spacecraft surfaces. Although the long wavelength Earth gravity field and the third body lunar and solar forces are well understood and modeled, SRP is more problematic. With latter day applications demanding orbital precisions at the level of a few centimeters, not only must SRP be accounted for, but also it must be modeled very accurately. Because of the complexity of the computational process, it has been difficult in the past to compute accurate analytical models for all but simply shaped spacecraft.

In recent years most research on SRP has concentrated on empirical modeling, for example, Refs. 1 and 2. These empirical models have been derived from the analysis of highly redundant systems comprising large networks of continually operating reference stations. These analyses often seek the perfect empirical parameterization for SRP. The problem here is that these empirical parameters tend to absorb partially all of the other unmodeled forces, many of which are nonconservative and have complex signatures. These force effects can include anisotropic thermal reradiation from the spacecraft body, albedo effects, small drag forces, space vehicle outgassing, and gravity field mismodeling. Hence, although the use of empirical parameters can cause the observations to fit very well to the model, they do not necessarily help to improve our understanding of the physical effects driving the orbit. Moreover, the larger is the number of empirical parameters included in the model, the weaker is the data strength of the final ephemeris. For operational

Received 13 February 2003; revision received 18 August 2003; accepted for publication 22 August 2003. Copyright © 2003 by the American Institute of Aeronautics and Astronautics, Inc. All rights reserved. Copies of this paper may be made for personal or internal use, on condition that the copier pay the \$10.00 per-copy fee to the Copyright Clearance Center, Inc., 222 Rosewood Drive, Danvers, MA 01923; include the code 0022-4650/04 \$10.00 in correspondence with the CCC.

\*Lecturer, Department of Geomatic Engineering.

systems attempting to predict orbits from a relatively small number of range observations, this can degrade the solution accuracy. More problematic for scientific applications such as Earth orientation estimation is the case when the empirical SRP parameters become correlated with other estimated model terms.

In contrast to empirical modeling, aside from Refs. 3–5, little work has been done on improving the a priori accuracy of SRP models. It may be that commercial companies do have tools to approach the modeling problem; however, there has been little published work that explains such methodologies in detail. The exception to this is Ref. 5, in which a technique based on splitting the spacecraft surface into triangular facets and carrying out shadowing analysis from one triangle to another is described. The current paper describes a new approach to the calculation of theoretical SRP models that attempts to overcome some old problems in this area. The aim is to account analytically for SRP as accurately as possible to free up the empirical parameters to probe the system dynamics for the next order of effects. Through a more thorough understanding of the system dynamics, the ability to predict the spacecraft trajectories will also improve, with associated gains in real-time performance such as operational oceanography and precise point positioning. Improving the accuracy of the predicted trajectory also speeds up the process of target acquisition for satellite laser ranging, thus, increasing the arc length over which the satellite can be tracked. Although no analytical model can be completely accurate, the approach advocated in this paper is also useful in that some attempt can be made to characterize the errors and, hence, derive a model for the process noise.

This paper presents the theoretical background to SRP modeling and goes on to describe the algorithms and functionality of a suite of software tools that have been developed for the purposes of computing high-precision analytical SRP models. The technique can be applied in the development of a system for simulation purposes, in the operational phase as part of the orbit prediction problem and in scientific analysis of system dynamics. With the modernization of existing GNSS, and the possibility of entirely new constellations of satellites, the development of the new method may be timely. This paper concentrates on the explanation of the modeling method, which has been developed considerably since its first use during the International GLONASS Experiment 1998 (IGEX-98) campaign to study the Russian GLONASS system.<sup>6</sup> The method has been developed to be applicable generally to any spacecraft, and is currently being applied to global positioning system (GPS) block IIR, JASON-1, and ENVISAT.

### Theoretical Background

The theoretical basis for radiation pressure was first proposed by the Scottish physicist James Clerk Maxwell in 1871.<sup>7</sup> Experimental evidence was shown in 1900 by the Russian physicist Pyotr Nikolaievich Lebedev and independently in 1901 by the Americans Nichols and Hull (see Ref. 7). Einstein's special theory of relativity provides for the relationship between energy, mass, and momentum:

$$\varepsilon = [(c_{EM}p)^2 + (m_0c_{EM}^2)^2]^{\frac{1}{2}} \quad (1)$$

For a photon  $m_0 = 0$ , and hence,  $\varepsilon = c_{EM}p$ . Einstein, building on ideas developed by Max Planck, also proposed a corpuscular theory of light in which each photon has an energy proportional to its frequency  $f$  such that  $\varepsilon = hf$ , where  $h$  is Planck's constant, which yields  $p = h\nu/c_{EM}$ . Thus, a photon's momentum is proportional to its frequency. If such a photon is absorbed by some surface, the momentum is transferred to the body. Hence,

$$p = hf/c_{EM} \quad (2)$$

Let the average number of solar photons of frequency  $f$ , striking the unit area of the surface per second at 1 astronomical unit (AU) be  $n(f)$ ; therefore,

$$\frac{dp_{n(f)}}{dt} = \frac{n(f)hf}{c_{EM}}$$

the change in momentum per unit area per unit time. Hence,  $dp_{n(f)}/dt$ , is the force per unit area due to photons of frequency  $f$ . Integrating over the solar electromagnetic spectrum, we have

$$F_{\text{due to incident radiation}} = \int_{\text{solar EM spectrum}} \left( \frac{h}{c_{EM}} \right) n(f) f df \quad (3)$$

However,

$$\int_{\text{solar EM spectrum}} hn(f) f df = E$$

where the solar irradiance  $E$  is in joules per second per square meter. Hence, at 1AU, force per unit area due to incident radiation is

$$F_{\text{due to incident radiation}} = E/c_{EM} \quad (4)$$

Equation (4) is the foundation of any attempt to model SRP analytically. Note that both terms on the right-hand side are very well determined. The speed of light in vacuum is a fundamental constant and requires no further discussion. The solar irradiance  $E$  is measured directly in space by a number of probes, for example, SOHO and GOES. High-accuracy measurement of the parameter is driven primarily by climate change research.<sup>8</sup>

Equation (4) gives the force acting on unit area due to absorbed radiation falling normally onto a surface as a function of the solar irradiance parameter. It can be shown (Appendix A) that this leads to the following functions, which model the force acting on a surface due to SRP:

$$F_{\hat{n}} = -P \left\{ (1 + \mu\nu) \cos \theta + \left( \frac{2}{3} \right) \nu (1 - \mu) \right\} \quad (5)$$

$$F_{\hat{s}} = P \{ (1 - \mu\nu) \sin \theta \} \quad (6)$$

Note that the two-thirds factor in Eq. (5) derives from the assumption of a Lambertian distribution for the diffusely reflected light. (See Appendix B for the derivation.)

### Spacecraft Attitude and Coordinate Systems

Spacecraft SRP variations are directly related to the time-varying orientation of the vehicle with respect to the sun. Fortunately, because solar radiation is the prime source of power for most near-Earth orbiters, their attitude behavior can often be modeled in a relatively simple way. GPS and GLONASS spacecraft maintain particular attitude characteristics for the majority of their mission lifetimes. The spacecraft solar panels are oriented nominally to be orthogonal to the vector from the spacecraft to the sun. The antenna boresight (Fig. 1) points toward the geocenter. The conventional definition for the spacecraft body-fixed system (BFS) basis has the origin at the nominal spacecraft center of mass. The Z axis is parallel to the antenna boresight, the Y axis points along one of the solar panel boom arms, and the X axis completes the right-handed set. Under normal

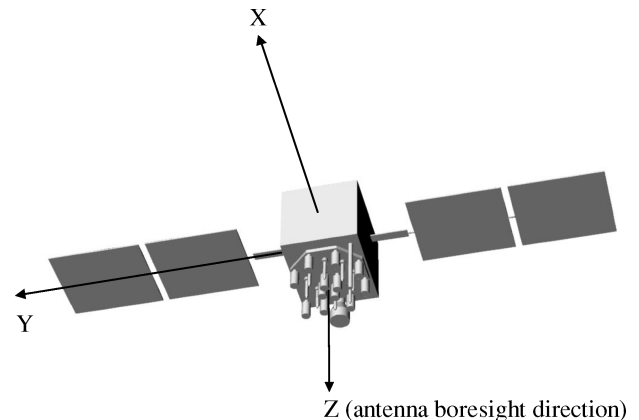


Fig. 1 Spacecraft body-fixed coordinate system.

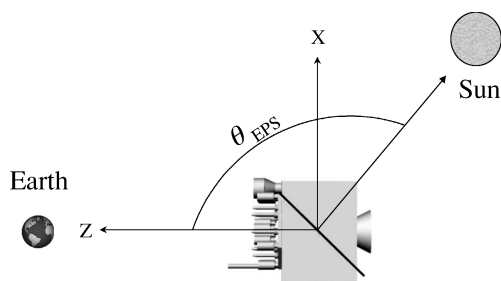


Fig. 2 EPS angle.

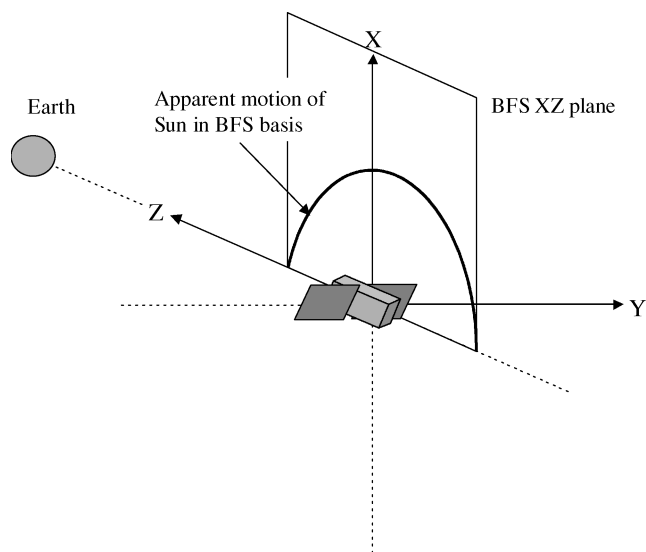


Fig. 3 Apparent motion of sun in GPS spacecraft BFS basis.

circumstances the sun is always in the same hemisphere (above the  $Y$ - $Z$  plane) as the  $X$  axis.

Given these attitude constraints, the BFS  $X$ - $Z$  plane nominally includes the sun and is, to first order, also a plane of symmetry for the spacecraft. As a result, the profile of the spacecraft presented to the sun over most of its mission lifetime varies uniquely as a function of the so-called Earth-probe-sun (EPS) angle. The EPS angle is between the BFS  $Z$  axis (which points to the Earth) and the probe-sun vector (Fig. 2).

In the BFS basis, the Earth would appear to be continually on the  $Z$  axis, and the sun would appear to rise and set in the  $X$ - $Z$  plane, never falling below the  $Y$ - $Z$  plane (Fig. 3). The only parts of the spacecraft apparently moving would be the solar panels, rotating about the  $Y$  axis as they track the sun. For these reasons, the BFS basis is the natural frame to use in modeling SRP effects. The attitude is driven by the requirements of spreading the satellite navigation signals evenly over the hemisphere presented to the spacecraft, while at the same time maximizing the solar radiation falling on the solar panels. There are instances where GPS spacecraft depart from this attitude and do not maintain their solar panels orthogonal to the photon flux. These effects are caused primarily by the satellite yaw behavior for low  $\beta$  angles. (The  $\beta$  angle is measured between the Earth-sun vector and the satellite orbital plane.) These issues will be discussed in a forthcoming paper by the group at University College London (UCL) on SRP modeling for the GPS block IIR spacecraft.

LEO spacecraft attitude modes are often far more complex than for GPS-type spacecraft. However, an important distinction is that the attitude of spacecraft such as TOPEX-POSEIDON and JASON-1 is measured to very high precision and that the attitude quaternions are made available to investigators. This knowledge of the time-varying attitude can be exploited to account accurately for radiation pressure effects. In contrast, for the higher altitude GPS and GLONASS spacecraft, we are forced to rely principally on attitude laws without knowing precisely how well the attitude control

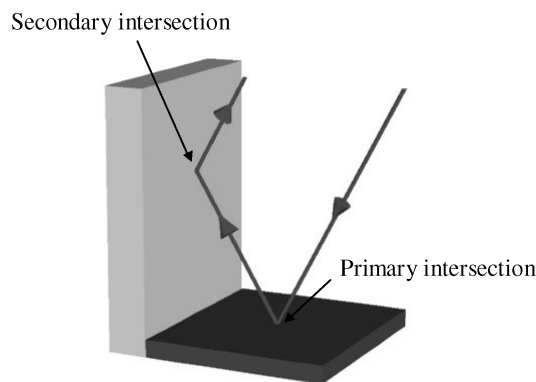


Fig. 4 Primary and secondary intersections.

subsystems are able to realize these models. This uncertainty as to the true attitude has caused some problems in the past for both orbit determination and positioning applications.<sup>9,10</sup>

To use Eqs. (5) and (6) to compute the SRP at some point in the orbit, the orientation of each part of the spacecraft with respect to the sun and the degree to which each part is cast into shadow must be known. Accurate calculation of each component's time-varying profile is obviously essential, but this is also a complicated task for real spacecraft. An associated second-order effect is what happens when light is reflected from one surface and then strikes another. This causes additional acceleration of the spacecraft. The problem has been noted in the literature,<sup>3</sup> but the effect has previously been impossible to quantify. For the purposes of this paper, the initial striking of the spacecraft by radiation is termed a primary intersection. The striking of another surface on reflection is termed a secondary intersection (Fig. 4).

### Core Elements of Algorithm

The basis of the method is described next. A more detailed description of the basic algorithm may be found in Ref. 6. Subsequently, some modifications to the original algorithm are introduced, which have radically improved the method.

### Spacecraft Description

The spacecraft surface is modeled as interlocking regular and irregular polygons, cylinders, circular and ring components, paraboloids, and cones (Fig. 5). The spacecraft structure source file includes the BFS coordinates of the vertices of the polygonal components, arranged such that the outward pointing normal to a component can be calculated unambiguously. Cylinders, paraboloids, and cones are treated differently; this is described later in the paper. Circular components are given by the circle center point and two other points on the circumference. Also included in the source file are the reflectivity and specular coefficients for each component.

In the spacecraft's orbit most of the structure is static in the BFS basis, apart from the solar panels. These rotate about the BFS  $Y$  axis, and their component vertices are recomputed automatically by the software dependent on the particular EPS geometry under consideration.

In the algorithm described in Ref. 6, cylindrical components were tessellated into many thin planar strips. This tessellation is carried out automatically by the algorithm. This vastly increased the number of components needed to model the structure and introduced an element of approximation that degraded the structural information available. The new method for modeling cylinders (and paraboloids and cones) given in the section on speed optimization retains the true native geometry and massively reduces the algorithm runtime.

### Modeling of the Photon Flux-Spacecraft Interaction

The underlying idea is to simulate the photon flux using a pixel array. The orientation of this array in the BFS basis is a function of the EPS angle (Figs. 2 and 6). Note that for LEO spacecraft, and for studies of the effects of nonnominal attitude for GNSS spacecraft,

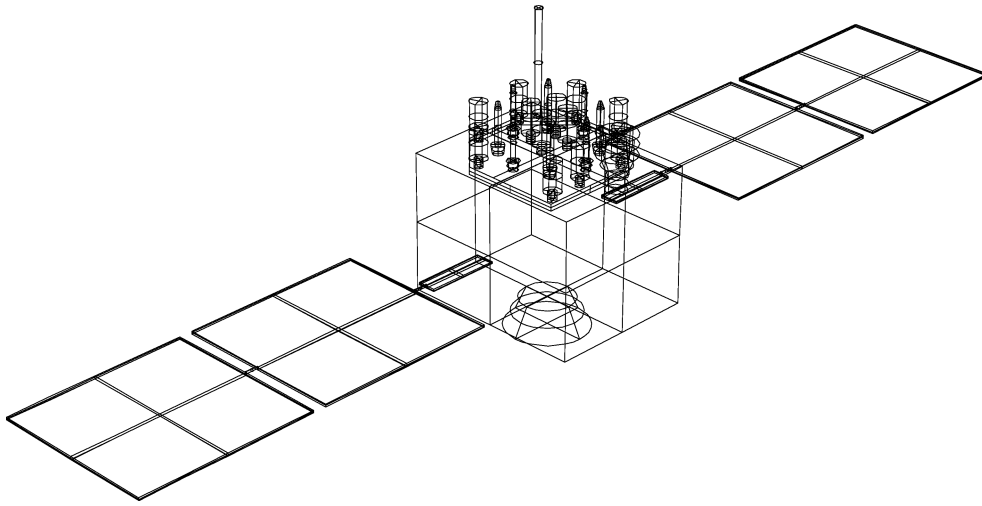


Fig. 5 Spacecraft structure broken down into geometric primitives.

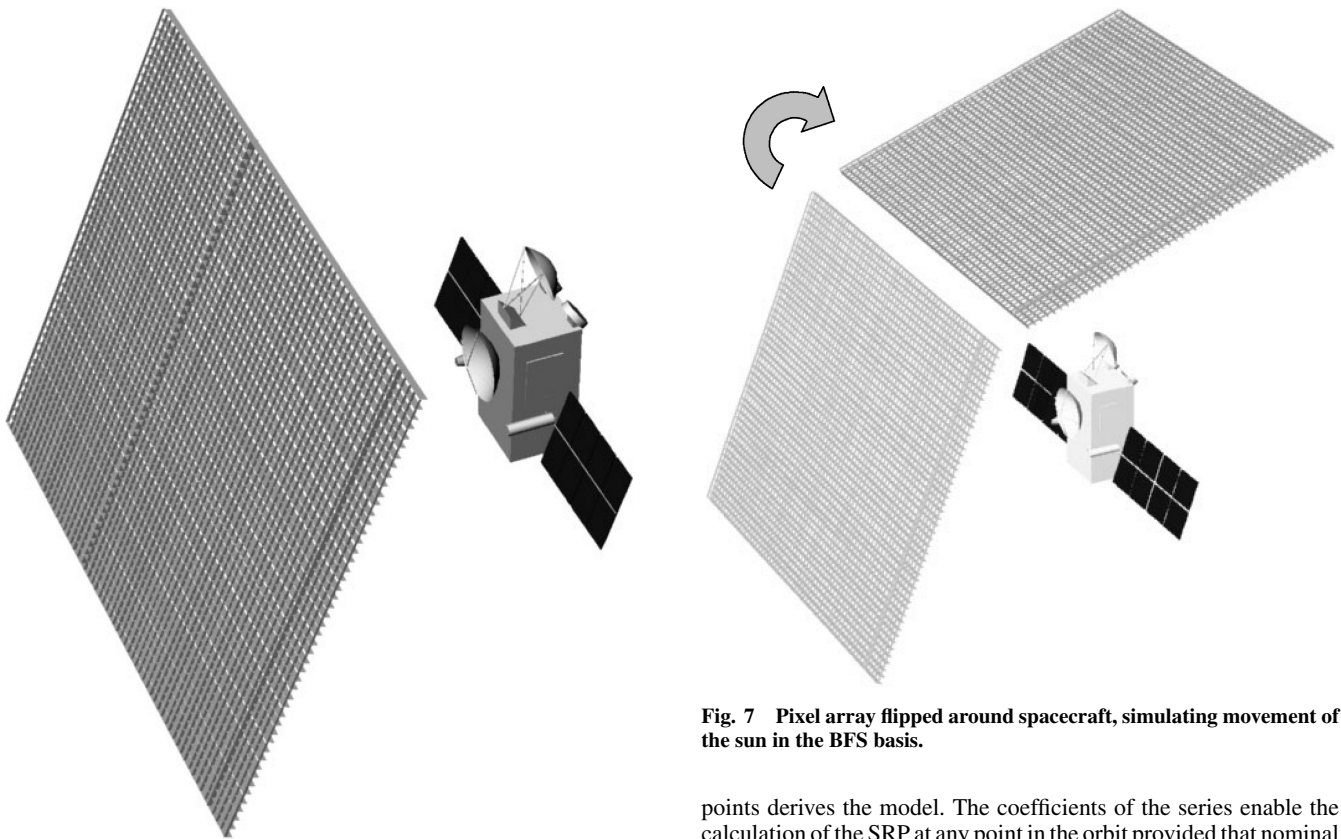


Fig. 6 Photon flux simulated with a pixel array.

the orientation of the pixel array in the BFS basis can be more complex, and this is explained in the section on nonnominal attitude. For any one orientation, the array is swept over the spacecraft simulation and used to calculate the resultant SRP force. The array is sequentially rotated around the spacecraft to simulate the variations in the EPS geometry and spacecraft attitude, with the solar panels adjusted accordingly (Fig. 7). The resultant force is divided by the spacecraft mass to give the acceleration, in the BFS at a number of discrete EPS angles. These accelerations are decomposed along the BFS  $X$ ,  $Y$  and  $Z$  axes. Note that in their nominal attitudes most GNSS spacecraft have no resultant component of the SRP acceleration acting along the  $Y$  axis. The variations in the  $X$ - and  $Z$ -axis accelerations can each be modeled as a periodic function, with the EPS angle as the independent variable. Hence, fitting a Fourier series to the data

Fig. 7 Pixel array flipped around spacecraft, simulating movement of the sun in the BFS basis.

points derives the model. The coefficients of the series enable the calculation of the SRP at any point in the orbit provided that nominal position vectors of the spacecraft and the sun are known. A different approach is adopted for LEO spacecraft, which can have attitude modes where the solar panels are not maintained orthogonal to the photon flux and have large components of the SRP acting along the  $Y$  axis.

The calculation for the resultant force at any particular EPS angle proceeds as follows. The pixel array plane is orthogonal to the vector from the spacecraft center of mass to the sun. The dimensions of the array are calculated by projecting the limits of the spacecraft profile onto the array plane. At the start of the process, the user must specify the resolution of the pixel array. This is the distance in millimeters between the center points of adjacent pixels. Each pixel is converted to a ray by adding, to the pixel's center point coordinates, the unit vector from the sun to the spacecraft. This gives two points on a straight line, which, along with the area of the pixel and the value for the solar irradiance, constitutes the light-ray model. These rays are projected, one by one, toward the spacecraft simulation, and a

test is carried out to determine which part (if any) of the spacecraft is struck. Each component of the spacecraft is tested for a possible intersection. For polygonal and circular components this consists of determining the intersection point of the ray and the component plane. A point-in-polygon test, adapted for three-dimensional geometry, then determines whether the intersection point is within the limits of the component. For all of the components that pass this test, the one with the shortest associated light path (that is, from the pixel center point to the intersection point on the component) is chosen as the part that is struck by the ray.

Equations (5) and (6) are then used to calculate the force acting on the spacecraft for that particular ray. In these equations, the angle of incidence is calculated from the scalar product of the incident ray vector and the component normal, and the  $A \cos \theta$  term is given by the area of the pixel. The process loops over all of the pixels in the array, summing the vector components of the forces. The output from this section is the force acting on the spacecraft at a particular EPS angle, due to primary intersections.

### Modeling of Secondary Intersection Effects

As already stated, the secondary intersection effect has, historically, been difficult to estimate. In the pixel array algorithm, ray-tracing functions were included to track the light path of the specularly reflected radiation. This approach was adopted because the specular component of the reflected light retains a sense of direction. Diffusely reflected radiation is isotropic over the surface of the hemisphere centered on the component intersection point and, as the name implies, becomes diffuse. This effect is mainly disregarded, although the software does include some basic modeling tools that enable the calculation of diffuse secondary intersection. The flux of radiation in the specularly reflected ray is then modeled by scaling the solar irradiance  $E$  by the product of the component's reflectivity and specularity,  $\mu v$ . The intersection point of the primary intersection is treated as the start point of the new ray. The direction of the reflected ray is constrained to be in the plane defined by the component normal and the incident light ray. After the reflected ray's start point and direction are defined, slightly modified versions of the tests outlined in the preceding section are carried out again to determine if a secondary intersection is possible. If there is a secondary intersection, the vector components of the resulting force are added to those of the primary intersection.

### Speed Optimization and Dealing with Geometric Primitives

The version of the software described in Ref. 6 used a tessellation technique to deal with cylinders and could not be used directly with spacecraft featuring paraboloid or conical components. To compute models for LEO spacecraft such as JASON-1 and ENVISAT, and also to decrease the runtime of program execution, several algorithms were developed that retain completely the structure of the components based on geometric primitives for cylinders, paraboloids, and cones.

The methods used to compute the intersection point of a ray of light and the surfaces of cones, paraboloids, and cylinders are similar, and the general principle is explained using a paraboloid as an example. The paraboloid is defined in the source file by the BFS position vectors of the center of the open end and the vertex, the radius of the open end, and whether it is inward or outward facing.

Initially the light ray, vector  $\mathbf{q}$  in Fig. 8, and the paraboloid can be in any relative orientation. In the following, the system comprises the position vectors of the paraboloid principal axis and the start- and endpoints of the normalized light ray vector. The geometry of the problem is then simplified by translating and rotating the system such that the principal axis of the paraboloid is coincident with the basis  $Z$  axis, and its open end is sitting on the  $X$ - $Y$  plane (Fig. 9). The system is then rotated around the  $Z$  axis until the light ray vector is in a plane parallel to the  $X$ - $Z$  plane. This set of transformations is given as follows:

1) Subtract  $\mathbf{x}_c$  from all system vectors, effectively dragging the center of the paraboloid open end to the basis origin. Once part 1 has been applied to the system vectors,  $\mathbf{x}_d$  becomes the axis vector of the paraboloid.

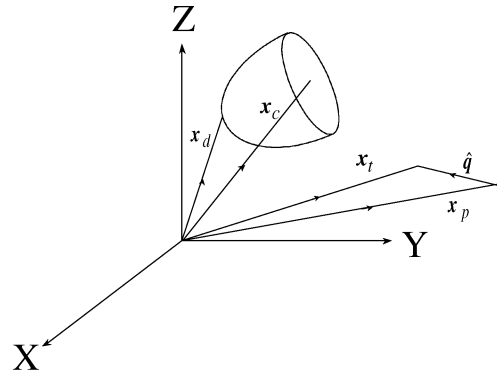


Fig. 8 Geometry of light ray incident on paraboloid.

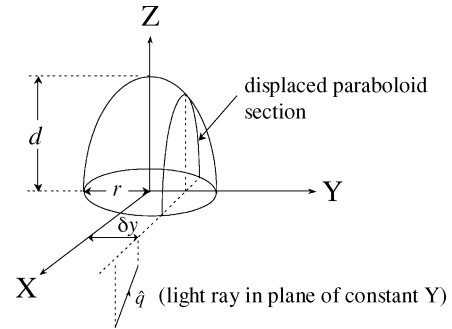


Fig. 9 Geometry of paraboloid problem in transformed system.

2) Solve for  $\omega$ , which is a rotation about the basis  $Z$  axis forcing the paraboloid axis into the  $X$ - $Z$  plane with an acute angle with respect to the  $X$  axis. Let  $\mathbf{x}_d - \mathbf{x}_c = \mathbf{x}'_d = x'_d i + y'_d j + z'_d k$ . Then  $\omega = \text{atan2}(y'_d, x'_d)$ , with screening for special cases. Apply

$$\mathbf{R}_\omega = \begin{bmatrix} \cos \omega & \sin \omega & 0 \\ -\sin \omega & \cos \omega & 0 \\ 0 & 0 & 1 \end{bmatrix} \quad (7a)$$

to  $\mathbf{x}'_d$ :

$$\mathbf{x}''_d = \mathbf{R}_\omega \mathbf{x}'_d \quad (7b)$$

3) Solve for rotation  $\varphi$ , acting about the  $Y$  axis to align  $\mathbf{x}''_d$  with the basis  $Z$  axis:  $\varphi = \text{atan2}(x''_d, z''_d)$ , again applying some logic to deal with special cases:

$$\mathbf{R}_\varphi = \begin{bmatrix} \cos \varphi & 0 & -\sin \varphi \\ 0 & 1 & 0 \\ \sin \varphi & 0 & \cos \varphi \end{bmatrix}$$

Hence, operate on  $\mathbf{x}_p$  and  $\mathbf{x}_t$ :

$$\mathbf{x}_p^{c\omega\varphi} = \mathbf{R}_\varphi \mathbf{R}_\omega (\mathbf{x}_p - \mathbf{x}_c) \quad (8)$$

$$\mathbf{x}_t^{c\omega\varphi} = \mathbf{R}_\varphi \mathbf{R}_\omega (\mathbf{x}_t - \mathbf{x}_c) \quad (9)$$

4) Solve for rotation  $\kappa$ , acting about the basis  $Z$  axis to bring the ray vector into a plane of constant  $Y$  values:

$$\kappa = \text{atan2}(y_p^{c\omega\varphi} - y_t^{c\omega\varphi}, x_p^{c\omega\varphi} - x_t^{c\omega\varphi}) \quad (10)$$

again screening for singularities. Hence, the full transformation procedure is

$$\mathbf{x}_s = \mathbf{R}_{\omega\varphi\kappa} (\mathbf{x}_i - \mathbf{x}_c) \quad (11)$$

where  $\mathbf{x}_i$  is the vector in the original basis,  $\mathbf{x}_s$  is the vector in the simplified basis, and

$$\mathbf{R}_{\omega\varphi\kappa} = \begin{bmatrix} \cos \kappa \cos \varphi \cos \omega - \sin \omega \sin \kappa & \cos \kappa \cos \varphi \sin \omega + \cos \omega \sin \kappa & -\sin \varphi \cos \kappa \\ -\sin \kappa \cos \varphi \cos \omega - \sin \omega \cos \kappa & \cos \kappa \cos \omega - \sin \omega \sin \kappa \cos \varphi & \sin \varphi \sin \kappa \\ \sin \varphi \cos \omega & \sin \varphi \sin \omega & \cos \varphi \end{bmatrix} \quad (12)$$

If an intersection is possible, the plane through the light ray parallel to the  $X$ - $Z$  plane now cuts the paraboloid (the displaced paraboloid section in Fig. 9). The problem of determining the intersection point is reduced to the solution of simultaneous equations of the displaced section locus and a straight line.

The procedure follows. Under the simplified geometry, a test can be used to terminate the process if necessary: If  $(\delta y > r)$ , this implies that the light ray misses the paraboloid. Note that  $\delta y$  is the distance between the  $X$ - $Z$  plane and the plane within which the ray vector is confined after the final system rotation [Eq. (10) and Fig. 9].

The process then proceeds by determining the parabola coefficients of the principal and displaced sections of the paraboloid (Fig. 9): The locus of the principal section of the paraboloid in the basis  $Z$ - $Y$  plane is

$$z = A_\lambda y^2 + C, \quad C = d, \quad A_\lambda = -d/r^2$$

The displaced section is parallel to the  $XZ$  plane, so that its locus can be modeled in terms of  $X$  and  $Z$  alone. Coefficients of displaced parabola are  $a$  and  $c$ .

The height of displaced section ( $c$ ; Fig. 10) is given by the  $Z$  value of the principal section at  $x = \delta y$ :

$$c = A_\lambda (\delta y)^2 + C$$

The roots of the displaced section locus are given by  $x_l$  (Fig. 10):

$$x_l = \sqrt{(r^2 - \delta y^2)}$$

and  $a = -c/x_l^2$ . Hence, the possible points of intersection on the paraboloid in the simplified basis are given by the equation of the straight line defined by the light ray and the parabola given by

$$z = ax^2 + c$$

Note that, depending on the relative geometry of the ray start-point and the displaced paraboloid section, a number of special cases must be dealt with. The actual intersection point is given by those coordinates that are closest to the ray start-point  $p$  along the positive direction of the ray vector.

Finally, the transformation computed to set up the simplified geometry is reversed to give the intersection-point coordinates in the spacecraft BFS basis. Let  $\mathbf{x}_k$  be the intersection point position vector in the simplified basis and  $\mathbf{x}_f$  the intersection point position vector in the original basis:

$$\mathbf{x}_f = [\mathbf{R}_\kappa \mathbf{R}_\varphi \mathbf{R}_\omega]^{-1} \mathbf{x}_k + \mathbf{x}_c$$

$\mathbf{R}_\kappa \mathbf{R}_\varphi \mathbf{R}_\omega$  is orthogonal; therefore, the inverse is simply the transpose. In the next step, once the intersection point is known, it is necessary to determine the normal to the paraboloid at that point.

From the perspective of algorithm performance, this treatment of the system geometry has an enormous effect on runtime. The GLONASS model computed at a pixel resolution of 10 mm in Ref. 6 took several days to compute, whereas when the preceding

technique was used, this computation was completed in under 2 h, both of these computations having been carried out on a 500-MHz processor using 500 MB of RAM. Moreover, the true geometry of each spacecraft component is retained, thereby also increasing the algorithm's accuracy as well as efficiency.

### Treatment of Nonnominal Attitude of GNSS Spacecraft and Adaptations for LEO Attitude Modes

The techniques described so far flip the pixel array around the spacecraft assuming that the sun is confined to the BFS  $XZ$  plane. Under some circumstances, GNSS spacecraft do not conform to this control law, resulting in nonnominal attitude. There are two reasons for tackling this problem. The first of these is largely historical and is related to the second, which is a more practical issue. Early research on GPS<sup>11</sup> showed that an anomalous force acting along the spacecraft  $Y$  axis, termed a  $Y$  bias, existed. A complete physical explanation for the  $Y$  bias is still a matter for research. Some investigators<sup>12</sup> have attempted to relate the  $Y$  bias to a bias in the spacecraft attitude system, solving for an angular misalignment from empirical analysis. In the absence of more sophisticated computational tools, in Ref. 12 a simplified spacecraft model is used (in this case, the solar panels alone). Hence, the first driver behind developing nonnominal attitude SRP modeling tools was to calculate precisely what  $Y$  bias would result from a given perturbation to the attitude. The second reason results from the deliberate application of a yaw bias<sup>10</sup> to the GPS block IIA constellation in between 1994 and 1995. This constant and predictable behavior causes both the bus and the solar panels to deviate from their nominal attitudes by small amounts. As mentioned earlier, for small  $\beta$  angles the rate at which the spacecraft is required to yaw to maintain nominal attitude exceeds the maximum possible yaw rate in certain cases. Under these circumstances, the solar panels are not maintained orthogonal to the photon flux.

LEO and other spacecraft have attitude modes that are far less constrained than the GPS/GLONASS model. In the BFS basis, the sun is not necessarily confined to the  $X$ - $Z$  plane. However, at least to first order, in most attitude modes the solar panels are oriented to maximize the amount of radiation that is incident on the panel. That is, they do the best they can. These considerations underpin the approach adopted for rotation of the pixel array away from the  $X$ - $Z$  plane, simulating more complex attitude modes.

The technique used initially rotates the solar panels to the position they would occupy were the sun in the  $X$ - $Z$  plane for a given EPS angle. From this position, a quaternion axis is defined in the  $X$ - $Z$  plane and parallel to the surface of the solar panels. The user supplies a perturbing angle  $\delta$ , which is used as the angle of rotation in the quaternion (Fig. 11). The resulting direction cosine matrix is then applied to each element of the pixel array defined by the EPS angle. This rotation has the effect of tilting the pixel array away from the solar panels. The panels, although not aligned orthogonal to the photon flux, will be, nevertheless, optimally aligned given the geometrical constraints.

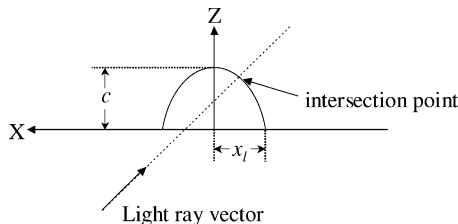


Fig. 10 Geometry of simplified system.

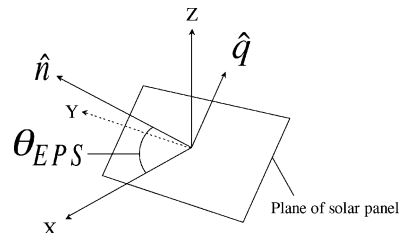


Fig. 11 Quaternion axis used in nonnominal attitude analysis.

The algorithm to compute the rotation matrix is quite compact:

$$\hat{q} = \begin{bmatrix} \cos \theta \\ 0 \\ -\sin \theta \end{bmatrix}, \quad \text{quaternion } \bar{b} = \begin{bmatrix} \hat{q} \sin(\delta/2) \\ \cos(\delta/2) \end{bmatrix} = \begin{bmatrix} b_1 \\ 0 \\ b_3 \\ b_4 \end{bmatrix}$$

Hence,

$$R_q(\theta, \delta) = \begin{bmatrix} b_1^2 + b_4^2 - b_3^2 & -2b_3b_4 & 2b_1b_3 \\ 2b_3b_4 & b_4^2 + b_1^2 - b_3^2 & -2b_1b_4 \\ 2b_1b_3 & 2b_1b_4 & b_3^2 + b_4^2 - b_1^2 \end{bmatrix}$$

Once the pixel array is rotated into position the computation is executed as per usual. The computed accelerations are stored as a function of the latitude and longitude of the sun in the BFS basis. This technique is particularly useful because it allows the pixel array to be positioned anywhere around the spacecraft to simulate the effect of the sun from that particular direction.

### Algorithm Validation

The algorithm is designed specifically to deal with complexity in the geometrical structure of the spacecraft, as well as the associated problems of shadowing, attitude variations and secondary intersections. There are thousands of lines of source code, and the coded operations are executed many millions of times as the pixel arrays are rotated around the spacecraft simulation. Under these circumstances, it is naturally difficult to guarantee that the software is doing exactly what it is supposed to be doing. Apart from the conventional testing of numerical stability in individual functions, two specific tests were used to validate the algorithm's precision.

The first test is carried out on the spacecraft simulation file. The pixel array is projected as per usual onto the structure. Each time that the software decides that a light ray has struck the spacecraft, the computed intersection point coordinates are written out to a text file. Subsequently this point cloud is imported into a three-dimensional graphics software, along with the geometrical primitives making up the spacecraft structure. This test showed that no spurious points off the spacecraft structure were found and that the algorithm treated all of the planar and curved surfaces appropriately. The technique was also applied to monitor the performance of the secondary intersection algorithm, with the same results (Figs. 12 and 13).

The second battery of tests used relatively simple combinations of components of a size and shape that might be found on a spacecraft. The response of these objects to the radiation environment was calculated directly from Eqs. (5) and (6) and then compared to the results obtained for the same objects using the algorithm. The structures were chosen to emphasise particular aspects of the algorithm such as shadowing, secondary intersections, and modeling of curved surfaces. In all cases, as the pixel resolution was gradually increased the two sets of figures converged (Fig. 14).

### Development of Model Representation

For any one position of the pixel array, an estimate of the response of the spacecraft to the modeled radiation flux can be made. As the pixel array is flipped around the spacecraft, a picture is built up of the response function at a series of discrete points. However, within any orbit determination process a continuous model is required. For GNSS-type spacecraft that keep the sun in their  $X$ - $Z$  planes, the model is computed by fitting a Fourier series to each of the  $X$  and  $Z$  accelerations data sets, using the EPS angle as the independent variable. A full three-dimensional model can be computed for each axis by fitting continuous surfaces to the  $X$ ,  $Y$ , and  $Z$  acceleration data by least-squares collocation and from this interpolating a grid

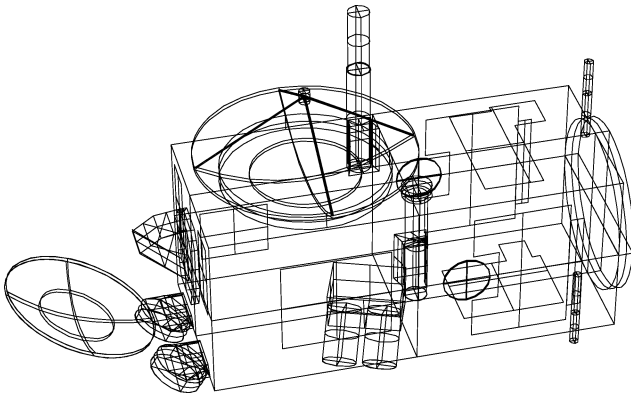


Fig. 12 Geometric primitive model of the JASON-1 bus.

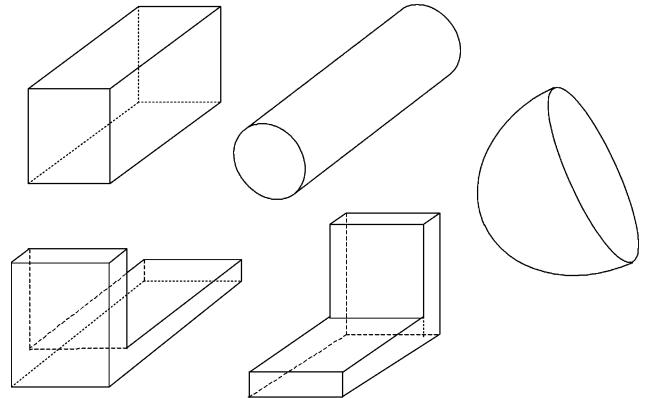


Fig. 14 Sample objects used in algorithm validation.

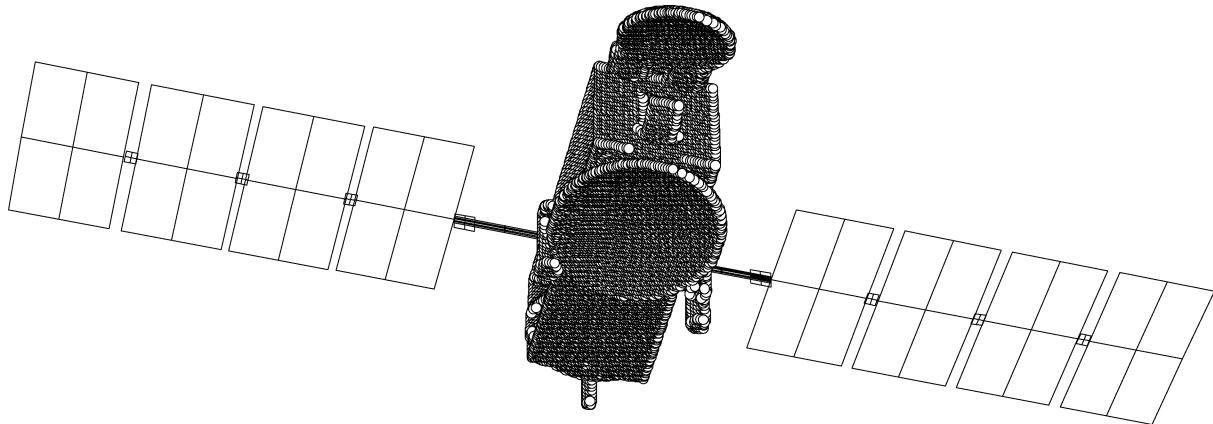


Fig. 13 Primary intersections from the JASON-1 bus analysis, at a coarse pixel resolution of 20 mm; note that the algorithm has correctly detected the spacecraft structure.

at 2.5-deg intervals. In this case, the independent variables are the latitude and longitude of the sun in the BFS basis. In application, given the BFS latitude and longitude of the sun, the  $X$ ,  $Y$ , and  $Z$  accelerations are computed by bilinear interpolation from the grid. The returned values must be scaled by the squared ratio of 1 AU to the actual probe–sun distance, to account for the varying solar irradiance.

### Model Testing and Results

The aim of this paper is to present, in as much detail as is practicable, the basis of the model computation method. In brief, Ref. 6 has results for the GLONASS models developed for the IGEX-98 campaign. The results were derived from long arc satellite laser ranging analysis. The pixel resolution for the models tested was 10 mm, with use of the older cylinder tessellation technique. RMS residuals for the 400-day arcs were 27.7 mm, and the model scale factors were in the range  $\pm 1\%$ , despite the relatively crude geometric data supplied for the spacecraft. Other tests showed that the models consistently outperformed a best-fitting box and wing model for both orbit prediction and estimation. Subsequent models using the methods outlined in this paper at a pixel resolution of 1 mm showed consistent improvements over the 10-mm resolution model. Forthcoming papers will discuss application of the method to JASON-1 and GPS block IIR.

### Discussion

For the problem of orbit prediction and constellation orbit design, the advantages of an analytical approach to SRP modeling are self-evident. However, in the case of orbit determination based on a statistical analysis process that combines dynamics and various forms of observable (SLR, DORIS, GPS, etc.), the advantages are less clear cut. The role that a good a priori analytical model plays here is that it furnishes the shape of the dynamic function from which the trajectory is finally derived, albeit with some empirical scaling or augmentation.

This paper does not address the related issues of thermal reradiation and albedo effects (taken here to also include long wavelength radiation emitted by the Earth). Although these effects are typically smaller than SRP forces by about two orders of magnitude for GNSS altitudes, they do require modeling for very high-accuracy applications. For LEO spacecraft, albedo effects can be very significant. The type of model that is computed using the techniques described in this paper can be brought to bear on the problem of albedo force modeling, in that the method can characterize successfully the profile of the spacecraft very precisely with respect to a given direction. However, the key obstacle when dealing with albedo is one of knowing what flux of radiation is arriving from a particular direction. This is the subject of ongoing research at UCL.

There are several sources of uncertainty in the described modeling process that can undermine the accuracy of the computed model. These uncertainties are related to spacecraft attitude, variations in the solar irradiance, coefficients of the optical properties of the spacecraft surface materials, and variations in the spacecraft mass.

For LEO spacecraft with multiple attitude measurement systems, uncertainties in the attitude are not, for the most part, an issue. The exact extent to which attitude variations for GNSS spacecraft limit the ability to model SRP a priori is a harder question to answer. The tools developed in this study can, at least, be brought to bear on the problem in answering the question of what anomalous forces would arise for a particular misalignment angle. In fact, this may be very useful in characterizing accurately the trade space between the precision (and cost) of the attitude determination and control system and the predictability of the orbit.

The solar irradiance is known to vary over a number of periods. The high-frequency component (x rays and gamma rays) related to solar rotation represents only a tiny fraction of the total solar irradiance (TSI) and can be safely ignored. Over the solar cycle, which has periods of between 9 and 14 years, the TSI varies by a range of 1.4 W/m<sup>2</sup>. This represents a maximum change of 0.1% over the whole cycle. The variation could be crudely modeled but

is unlikely to yield any great benefit over short arc analysis. Some gains may be realized over longer arcs.

The optical properties of the surface materials can be very difficult to acquire from the spacecraft manufacturer in the first place. This is a trying state of affairs in that these coefficients have a strong effect on the computed models and the subsequent orbit determination. The manufacturer should have, at the very least, a requirement to supply the mission analysis team the material types that were used in the construction. Frequently the optical properties quoted in manuals are quite crude, and further research is needed in this area to improve knowledge of both properties and associated uncertainties. A related problem is the gradual change in the surface of the spacecraft due to space weathering. Having said this, even using relatively crude values (such as those used in Ref. 6) can give good results.

The model of the interaction of the incident radiation and the surface of the satellite is rather simplistic (although it is something of an industry standard). It may be possible, in due course, to refine the technique by the use of a more sophisticated model that reflects more accurately the distribution of the reflected radiation. It may also be possible to validate such a model by laboratory measurements of the intensity of reflected radiation from a laser source.

Last, the gradual burning of fuel can change the location of the spacecraft center of gravity, and obviously it changes the area-to-mass ratio. Provided that the mass consumption is known, the a priori model can be largely corrected by scaling.

### Conclusions

This paper has presented the theoretical background and algorithm structure for a new method of computing high-precision, analytical solar radiation pressure models for GNSS and LEO spacecraft.

The technique can be usefully applied at the stages of design, operation, and postprocessed scientific analysis.

The computation process is automated and is designed to cope efficiently with the complexities of real spacecraft without having to make simplifying assumptions. Once the spacecraft structure has been designed, it is very straightforward to carry out the model computation. If there are adaptations to the design, their impact on the surface force modeling is easy to assess. The approach is highly cost effective. Validation techniques have been used to prove that despite the complexity of the software and that it is designed to deal with realistic spacecraft structures, it does deliver models that are accurate and true with respect to the source data used.

The force model effects of departure from nominal attitude for GNSS spacecraft can be assessed accurately with the algorithm in a way that was previously impossible. In turn, this enables the characterization of the trade space between more sophisticated (and expensive) attitude control and limitations in orbit prediction.

The key aspect of the method is that optimal use is made of what data are available for the spacecraft structure in characterizing the mathematical form of the radiation pressure surface force model.

### Appendix A: Derivation of Normal and Shear Force Expressions

The proportion of incident radiation that is reflected specularly is  $\mu\nu$ . The proportion of incident radiation that is reflected diffusely is  $\nu(1 - \mu)$ . The radiation incident on the surface is equal to  $E\text{Acos}\theta$ . Hence, from Eq. (4), the force due to direct radiation pressure  $F_{dp} = EA \cos \theta / c_{EM}$ .

Radiation that is reflected specularly from the surface gives rise to a reactive force along the opposite direction to the path of the reflected radiation. Therefore, the force due to specularly reflected radiation  $F_{sp} = \nu\mu EA \cos \theta / c_{EM}$ .

Of the radiation that is reflected diffusely, two-thirds contributes to a force normal to the surface, as shown in Appendix B. As for the specular force, this normal force is a reactive force and acts along the negative direction of the outward pointing normal to the surface. It is assumed (in this model) that the remaining diffusely reflected radiation is distributed evenly in azimuth, and hence, the summed



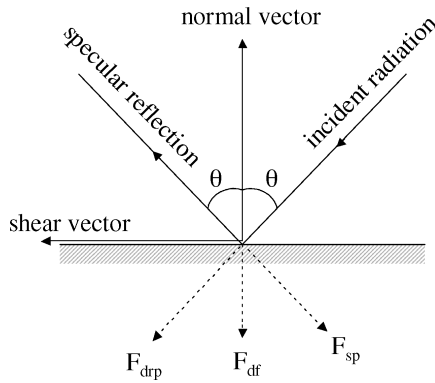


Fig. A1 Geometry of incident radiation/surface interaction.

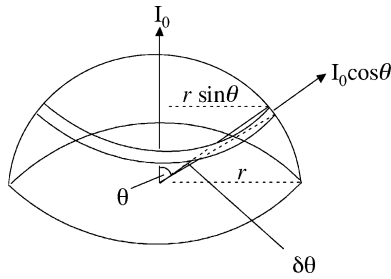


Fig. B1 Lambert diffuse reflector geometry.

force effects are zero, which leaves only a normal force component to consider.

Hence, force due to diffusely reflected radiation  $F_{df} = \left(\frac{2}{3}\right)\nu(1-\mu)EA \cos \theta / c_{EM}$ . Resolving these forces normal and shear (see Fig. A1 for these directions) to the surface gives

$$F_n = -(AE \cos \theta / c_{EM}) \left\{ (1 + \nu\mu) \cos \theta + \left(\frac{2}{3}\right)\nu(1 - \mu) \right\}$$

$$F_s = (AE \cos \theta / c_{EM})(1 - \nu\mu) \sin \theta$$

## Appendix B: Derivation of Two-Thirds Factor of Proportionality in Equation (5)

The problem is to calculate the proportion of diffusely reflected radiation that is emitted normal to surface. The Lambert assumption (Fig. B1) is that the intensity of radiation falls off by a factor of  $\cos \theta$  away from the normal to the surface. Let the intensity of radiation normal to surface above the point of emission be equal to  $I_0$ . The intensity of radiation through strip at colatitude  $\theta$  is constant,  $I_0(\theta) = I_0 \cos \theta$ . The radiation through strip is equal to

$$I_0 \cos \theta 2\pi r \sin \theta r \delta \theta \quad (B1)$$

The force due to the emitted radiation can be decomposed for each element of the strip normal and parallel to the surface. Because of the assumed symmetry, all of the force components parallel to the

surface summed for any one strip will sum to zero, which leaves a resultant force normal to the surface only.

The component of the radiation for one strip resolved normal to the surface would be

$$I_0 \cos \theta 2\pi r \sin \theta r \delta \theta \cos \theta \quad (B2)$$

The proportion of the radiation force components that is normal to the surface is the integral of component (B2) over the surrounding hemisphere divided by the integral of component (B1) over the same surface. The required proportion is

$$I_0 \int_0^{\pi/2} 2\pi r^2 \cos^2 \theta \sin \theta d\theta \bigg/ I_0 \int_0^{\pi/2} 2\pi r^2 \cos \theta \sin \theta d\theta = \frac{I_1}{I_2}$$

$$I_1 = \frac{2}{3} I_0 \pi r^2, \quad I_2 = I_0 \pi r^2$$

Therefore, the required proportion is equal to two-thirds. Note that only the component of the diffuse radiation force normal to the surface is nonzero

## References

- <sup>1</sup>Vigue, Y., Lichten, S. M., Muellerschoen, R. J., Blewitt, G., and Heflin, M. B., "Improved GPS Solar Radiation Pressure Modeling for Precise Orbit Determination," *Journal of Spacecraft and Rockets*, Vol. 31, No. 5, 1994, pp. 830–833.
- <sup>2</sup>Springer, T., Beutler, G., and Rothacher, M., "Improving the Orbit Estimates of GPS Satellites," *Journal of Geodesy*, Vol. 73, No. 3, 1999, pp. 147–157.
- <sup>3</sup>Fliegel, H. F., Gallini, T. E., and Swift, E. R., "Global Positioning System Radiation Force Model for Geodetic Applications," *Journal of Geophysical Research*, Vol. 97, No. B1, 1992, pp. 559–568.
- <sup>4</sup>Fliegel, H. F., and Gallini, T. E., "Solar force Modeling of Block IIR Global Positioning System Satellites," *Journal of Spacecraft and Rockets*, Vol. 33, No. 6, 1996, pp. 863–866.
- <sup>5</sup>Marquis, W., and Krier, C., "Examination of the GPS Block IIR Solar Pressure Model," Proceedings of ION GPS 2000, Inst. of Navigation, 2000.
- <sup>6</sup>Ziebart, M., and Dare, P., "Analytical Solar Radiation Pressure Model for GLONASS Using a Pixel Array," *Journal of Geodesy*, Vol. 75, No. 11, 2001, pp. 587–599.
- <sup>7</sup>Semat, H., and Albright, J. R., *Introduction to Atomic and Nuclear Physics*, 5th ed., Rinehart and Winston, New York, 1972.
- <sup>8</sup>Frolich, C., and Lean, J., "The Sun's Total Irradiance: Cycles, Trends and Related Climate Change Uncertainties Since 1976," *Geophysical Research Letters*, Vol. 25, No. 23, 1998, pp. 4377–4380.
- <sup>9</sup>Bar-Sever, Y., Bertiger, W., Davis, E., and Anselmi, J., "Fixing the GPS Bad Attitude: Modeling GPS Satellite Yaw During Eclipse Seasons," *Navigation*, Vol. 43, No. 1, 1996, pp. 25–39.
- <sup>10</sup>Bar-Sever, Y. E., "A New Model for GPS Yaw Attitude," *Journal of Geodesy*, Vol. 70, No. 11, 1996, pp. 714–723.
- <sup>11</sup>Lichten, S. M., and Border, J. S., "Strategies for High-Precision Global Positioning System Orbit Determination," *Journal of Geophysical Research*, Vol. 92, No. B12, 1987, pp. 12,751–12,762.
- <sup>12</sup>Kuang, D., Rim, H. J., Schutz, B. E., and Abusali, P. A. M., "Modeling GPS Satellite Attitude Variation for Precise Orbit Determination," *Journal of Geodesy*, Vol. 70, No. 9, 1996, pp. 572–580.

A. Ketsdever  
Associate Editor